

Automated Detection of Cribriform Growth Patterns in Prostate Histology Images

Pierre Ambrosini^{1,*}, Eva Hollemans², Charlotte F. Kweldam², Geert J. L. H. van Leenders², Sjoerd Stallinga^{1,+}, and Frans Vos^{1,3,+}

¹Department of Imaging Physics, Faculty of Applied Sciences, Delft University of Technology, Delft, The Netherlands

²Department of Pathology, Erasmus University Medical Center, Rotterdam, The Netherlands

³Department of Radiology, Academic Medical Center, Amsterdam, The Netherlands

*p.ambrosini@tudelft.nl

+These authors contributed equally to this work

ABSTRACT

Cribriform growth patterns in prostate carcinoma are associated with poor prognosis. We aimed to introduce a deep learning method to detect such patterns automatically. To do so, convolutional neural network was trained to detect cribriform growth patterns on 128 prostate needle biopsies. Ensemble learning taking into account other tumor growth patterns during training was used to cope with heterogeneous and limited tumor tissue occurrences. ROC and FROC analyses were applied to assess network performance regarding detection of biopsies harboring cribriform growth pattern. The ROC analysis yielded an area under the curve up to 0.82. FROC analysis demonstrated a sensitivity of 0.9 for regions larger than 0.0150 mm² with on average 6.8 false positives. To benchmark method performance for intra-observer annotation variability, false positive and negative detections were re-evaluated by the pathologists. Pathologists considered 9% of the false positive regions as cribriform, and 11% as possibly cribriform; 44% of the false negative regions were not annotated as cribriform. As a final experiment, the network was also applied on a dataset of 60 biopsy regions annotated by 23 pathologists. With the cut-off reaching highest sensitivity, all images annotated as cribriform by at least 7/23 of the pathologists, were all detected as cribriform by the network. In conclusion, the proposed deep learning method has high sensitivity for detecting cribriform growth patterns at the expense of a limited number of false positives. It can detect cribriform regions that are labelled as such by at least a minority of pathologists. Therefore, it could assist clinical decision making by suggesting suspicious regions.

Introduction

Prostate cancer is one of the most common cancer types in men: about one man in 9 is diagnosed with prostate cancer in his lifetime¹. Histological image analysis of biopsy specimens is generally considered the reference standard for detection and grading of prostate cancer. The Gleason grading system is often used in practice to evaluate the severity of prostate cancer. The Gleason system distinguishes five basic architectural growth patterns, numbered Gleason grade G1 to G5. Presently, combinations of prevalent growth patterns are usually considered which is reflected in the Gleason Score and Grade Group (Table 1). However, in spite of such updates the current system is still associated with high inter-observer variability². For example, the classification between Grade Group 2 and 3 (Gleason Score 3 + 4 = 7 and 4 + 3 = 7) is often subject to disagreement among pathologists. The classification between these two Grade Groups is highly relevant since it influences therapeutic decision-making. Actually, each individual Gleason grade is a collection of different growth patterns (Fig. 1). Particularly, Gleason grade 4 comprises glands forming cribriform, glomeruloid, ill-defined, fused, and complex fused growth patterns^{3,4}. Unfortunately, the disagreement among pathologists is also relatively high regarding the sub-type classification.

In a recent inter-observer study, high consensus, i.e. 80% agreement among 23 pathologists, was reported on 23% of the cribriform cases, but rarely on fused and never on ill-defined patterns⁵. At the same time it was found that presence of cribriform growth patterns in prostate cancer imply a poor prognosis^{6–8}. The cribriform growth pattern could therefore be an important prognostic marker and its detection might add valuable information on top of the Gleason grading system.

Many clinical decisions have to be made during the treatment of prostate cancer patients, often by multidisciplinary teams or tumor boards. These decisions are complex due to the increasing number of available parameters e.g. from radiological imaging, pathology and genomics. There is a clinical need for technology that enables objective, reproducible quantification of imaging features. Specifically, automatic qualification of the biopsies regarding the Gleason grade and biomarkers derived from automated detection of cribriform glands would add objective parameters in a clinical decision support algorithm. Such automated detection tools can also bring visualization support to aid clinical decision-making.

We propose a method to automatically detect cribriform glands in prostate biopsy images. As the annotation of cribriform

glands is subject to intra- and inter-observer variability, erroneous cases will be re-evaluated by the original annotators and the algorithm's performance will be compared against the assessments of a large group of pathologists.

Engineered feature based machine learning approaches were used to identify stroma, benign and cancerous tissue for radical prostatectomy tissue slides⁹. Automatic Gleason grading were proposed as well using multi-expert annotations and multi-scale features based methods¹⁰. Additionally, deep learning methods have proven useful in digital pathology for various tasks such as detection and segmentation of glands, epithelium, stroma, cell nuclei and mitosis¹¹. This is relevant as such tissue segmentations can be a first step to a more detailed characterization. More recently, a variety of CNN-based methods were also used to classify prostate cancer tissue. These approaches differed regarding the type of histological images: Tissue Micro-Arrays (TMAs)¹² and Whole Slide Images (WSIs)^{13,14} acquired after radical prostatectomy versus WSIs obtained from prostate needle biopsies. Biopsy interpretation is challenging, though, due to the narrow tissue width since typically a needle diameter of around 1 mm is used. Importantly, assessment of needle biopsies can have impact on management of individual patients. Previously, segmentation and classification methods for automatic processing of prostate needle biopsies were developed to detect malignant tissue^{15,16}, as well as for partial^{17,18} and full Grade Group classification¹⁹. Automated detection of cribriform growth patterns in prostate biopsy tissue has, to the best of our knowledge, not yet been studied. Indeed, Gertych et al.²⁰ proposed a CNN combined with a soft-voting method to automatically distinguish four growth patterns including the cribriform growth pattern, but this was applied to lung tissue samples only. Moreover, it was stated that the method had only moderate recognition performance (F1-score=0.61) with regards to the cribriform growth pattern.

In order to assist pathologists and support clinical decision making, we aim to introduce a method for automatic detection of cribriform growth patterns. In summary, this paper presents the following contributions:

- Cribriform growth patterns are automatically detected and segmented from tissue slides obtained from prostate needle biopsies.
- Annotations of erroneous cases are re-considered to account for intra-observer variability.
- Algorithm performance is compared against assessments by a large group of pathologists.

Gleason grade	1,2 or 3	3 + 4	4 + 3	4 + 4	3 + 5	5 + 3	4 + 5	5 + 4	5 + 5
Gleason Score	≤ 6	7	7	8	8	8	9	9	10
Grade Group	1	2	3	4	4	4	5	5	5

Table 1. The Gleason grading system. A prostate specimen is classified in Gleason grade 1 to 5². The Gleason Score of a tissue is the sum of the primary Gleason grade and the secondary Gleason grade (in terms of predominance). In order to differentiate tissues with Gleason Score 7 = 3 + 4 and 7 = 4 + 3, Grade Group classification was introduced, replacing the Gleason Score.

Materials and methods

Neural network model

A convolutional neural network (CNN) was used to segment cribriform growth patterns in prostate biopsies stained with hematoxylin and eosin (H&E). The network took as input $x(i)$ an 1024x1024 pixels RGB colored biopsy region, with i indexing a particular pixel. The pixel sizes were 0.92x0.92 $\mu\text{m}^2/\text{pixel}$ in all cases (see *Experiments* section). In order to better discriminate between cribriform and other G4 growth patterns, the network was trained to additionally detect other G3 and G4 tissue types. Accordingly, the output consisted of 7 probabilities $\hat{y}^l(i)$ where $l \in L$ being one of the following labels: non-labelled, G3, G4 fused, G4 ill-defined, G4 complex fused, G4 glomeruloid and G4 cribriform. The non-labelled class was included to represent the non-tissue background and any other non G3 and G4 tissue (healthy tissue, G5, mucinous, perineural growth...).

Henceforth, $y^l(i)$ represents the reference label, which consists of 7 masks, again with i indexing a particular pixel. Each such reference label contained a 1 for one particular class and 0 for all other classes.

The Dice coefficient which quantifies positive overlap between label and prediction was used as loss function to be minimized during training of the network. With a batch of P images, the loss was defined as:

$$\mathcal{L}_D = -\frac{1}{P} \sum_{p=1}^P \left(\sum_{l \in L} w_l \frac{2 \sum_i y_p^l(i) \hat{y}_p^l(i)}{\sum_i (y_p^l(i) + \hat{y}_p^l(i)) + \epsilon} \right) \quad (1)$$

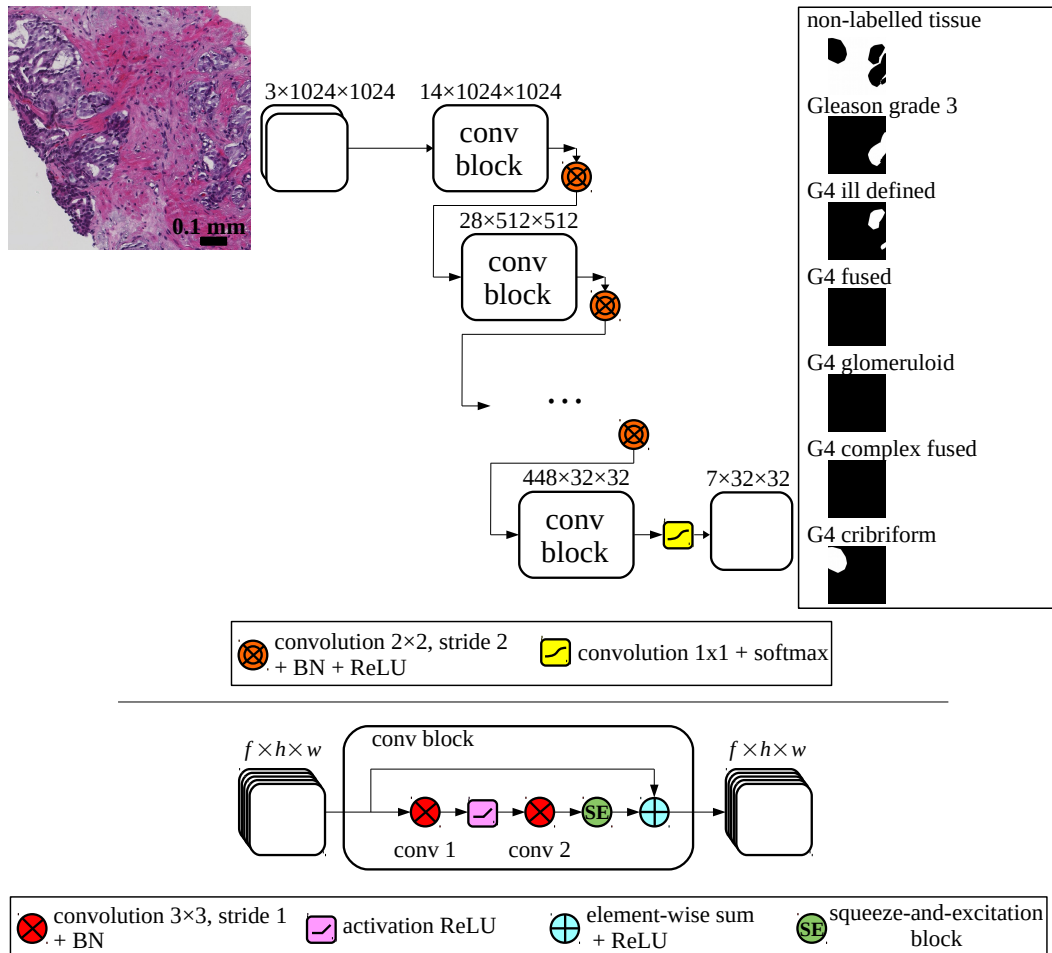
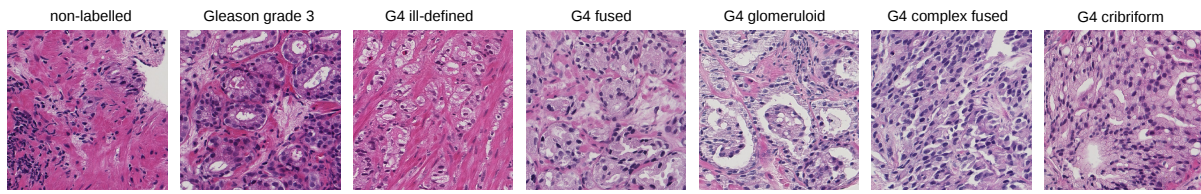


Figure 1. (top) Examples of different biopsy tissues with glands classified as Gleason grade 3 or 4.

(bottom) Deep convolutional neural network architecture: a biopsy patch image is fed into the network and the output after a softmax normalization is composed of 7 segmentation maps 32 times smaller than the input. The network is composed of 6 consecutive *conv blocks*. A *conv block* consists of 2 consecutive convolutions of input features (f feature maps of height h and width w) with a squeeze-and-excitation block and a residual connection. Downsampling is done using strided convolutions with a kernel 2x2, after which batch normalization (BN) and an activation rectifier linear unit (ReLU) are applied.

in which w_l is a weight associated with tissue label l . Our goal was to detect the cribriform growth pattern and therefore we used for that tissue a higher weight. Note that the other labels were included in the loss function only to obtain a better convergence during the training of the neural network. Practically, a weight of 0.4 was applied for the cribriform label and 0.1 to all other labels (so that weights sum to 1).

Details of the network architecture are depicted in Fig. 1. The design was based on the following two criteria. First, we focused on coarse cribriform growth pattern localization. Therefore, the resolution of the segmented output did not have to be as high as the original 1024x1024 input resolution. Instead, the outputs were masks of 32x32 pixels, which was sufficient to segment the smallest relevant glands. Accordingly, the 1024x1024 reference masks were downsampled to 32x32 in order to match the output of the neural network using standard averaging. Second, we wanted to achieve fast convergence and simultaneously accurate training. To accomplish this we applied several architectural features that have been shown to enhance training efficiency: residual connections with every convolution block²¹, 2x2 strided convolutions effectively learning to downsample²² and squeeze-and-excitation blocks for adaptively weighting channels in the convolution blocks²³. The output of the network was not post-processed afterwards.

Implementation

In order to have representative training data with each iteration of back-propagation, we made sure that a training batch of images always contained all the 7 possible labels. Accordingly, the batch size of the neural network was chosen to be the size of the label set $L = 7$.

Every network was initialized with weights randomly sampled from a uniform distribution²⁴ and trained during 60000 iterations with the stochastic gradient descent optimizer with a learning rate of 0.01, a decay of 5×10^{-4} and a momentum of 0.99. No explicit stopping criterion was included. Instead a validation set was used to choose optimal weights according to a metric as specified in the *Experiments* section. We used the Titan Xp and GTX 1080 Ti GPU's from Nvidia Inc. to perform the experiments.

To avoid over-training and add more variability in the training set, on-the-fly data augmentation was performed on each input patch. Input patches with their associated label masks were randomly vertically and/or horizontally flipped, translated in the range of $\pm 10\%$ of the image size, rotated (around the image center) in a range of ± 5 degrees and scaled with a factor in the range of 0.9 to 1.1. In histopathology, the staining method with H&E can result in different image contrasts. Therefore, after normalizing the RGB values (yielding values for each channel between 0 and 1) a random intensity shift was globally applied to each color channel of every image with a magnitude in the range of ± 0.05 . Furthermore, the range of the intensity in each channel was also randomly scaled between $\min \in [0, 0.1]$ and $\max \in [0.9, 1]$.

Experiments

The proposed network was trained and tested on an annotated biopsy dataset. However, cribriform growth pattern detection by pathologists themselves is not a trivial task. Consequently, uncertainties in the annotations occur, which hinders the training of the network. Therefore we let the misclassified biopsy regions by the algorithm in the previous experiment be annotated for a second time by the same pathologist. We did this for a detailed assessment of the misclassifications of the neural network, but also to quantify the reproducibility of annotating the growth patterns. Moreover, the image dataset from an extensive inter-observer study⁵ was used to evaluate our network in comparison to the assessment by 23 pathologists.

Cribriform detection performance

The CNN was first trained and tested on a dataset of prostate tissue images from 128 biopsies (one WSI per biopsy; one biopsy per patient) acquired by the department of Pathology of Erasmus University Medical Center, Rotterdam, The Netherlands. We selected only one WSI per patient in order to include data from as many patients as possible for an acceptable processing time. These data concerned clinical prostate biopsies from 2010 to 2016 with acinar adenocarcinoma cancer and a Gleason Score 6 or higher. From each patient, the biopsy with the most tumor volume was selected. 132 biopsies were digitized after which 4 of them were excluded due to severe artefacts and too little tumor tissue. The biopsies were stained with H&E and digitized using a NanoZoomer digital slide scanner (Hamamatsu Photonics, Hamamatsu City, Japan). The resulting images had a resolution of 0.23 $\mu\text{m}/\text{pixel}$. Two genitourinary pathologists sat together and annotated in consensus the different regions of each biopsy using the ASAP software²⁵. Subsequently, a label $l \in L$ was assigned to each such region according to the updated standard classification^{3,4}. The biopsies contained mainly G3 and G4 carcinoma. G5, mucinous differentiation, perineural growth and prostatic intraepithelial neoplasia were also present in respectively 6, 6, 1 and 1 biopsy slides. These rare tissues were assigned to the non-labelled group.

To discard the background region from the samples, a thresholding procedure was applied to the optical density transforma-

tion of the RGB channels¹⁵:

$$OD_c = -\log_{10} \frac{I_c}{I_{\max}} \quad (2)$$

where OD_c is the optical density of the channel c , I_c is the initial intensity and I_{\max} is the maximum intensity measured for the concerned channel. We found that the background was easily identifiable by $OD_c < 0.12$ in any of the channels.

Subsequently, each biopsy was downsampled to a resolution of $0.92 \mu\text{m}/\text{pixel}$ (i.e. by a factor 4 from the acquisition resolution) and subdivided in half-overlapping patches of 1024×1024 pixels (thus, taking steps of 512 pixels). Patches with more than 99.5% of background were discarded. For training, all remaining patches from each biopsy in the training set were shuffled and fed to the CNN while making sure that all classes were present (see *Implementation* section). During testing, all the patches of a test biopsy image were inferred by the CNN. Subsequently, to reassemble the full biopsy segmentation, only the 512×512 region in the center of each patch was kept in order to avoid overlapping segmentations. Also, we expected that the center part would yield the best classification accuracy as there is more context around it compared to the periphery of the patch.

An 8-fold cross-validation training scheme was applied. The 128 prostate biopsy images were therefore distributed over 8 groups (see Table 2). As detection of cribriform growth pattern is the focus of this study, the biopsies were first partitioned such that the cribriform annotations were uniformly distributed. Subsequently, the remaining biopsies were split up in a way to yield an approximately equal distribution of labels. This was done by means of the bin packing algorithm²⁶.

In each fold, 6 groups of images were used to train the network. Furthermore, one group was taken as a validation set to select the optimal neural network weights from all the weights saved after each epoch of training. The metric V to do so was a combination of the Dice function \mathcal{L}_D (eq.1) and also the specificity in order to minimize false positives:

$$V = \alpha \mathcal{L}_D + (1 - \alpha) \mathcal{L}_S \quad (3)$$

where $\alpha \in [0, 1]$ is a weight factor that balances the two terms; \mathcal{L}_S is the negative average pixel specificity of a batch of P images:

$$\mathcal{L}_S = -\frac{1}{P} \sum_{p=1}^P \left(\sum_{i \in \mathcal{L}} w_i \frac{\sum_i (1 - y_p^i(i))(1 - \hat{y}_p^i(i))}{\sum_i (1 - \hat{y}_p^i(i)) + \epsilon} \right) \quad (4)$$

Within each fold the network was trained four times during which patches were randomly shuffled to yield an altered training order. Furthermore, four weights were applied in the validation metric V : $\alpha \in [0.2, 0.3, 0.4, 1]$. Empirically, we found that any $\alpha > 0.4$ yielded the same weights as the Dice-only metric \mathcal{L}_D ($\alpha = 1$). In total 16 (=4*4) networks per fold were trained. In addition, an ensemble classifier was defined as the normalized sum of the predictions of the 16 networks.

The remaining group (of 8) served as the test set to evaluate the performance of the 16 networks as well as the ensemble network. The results of the 8 test sets (8 folds) were taken together to calculate a final performance measure (i.e. based on all the 128 biopsies).

From the predictions, i.e. the probability maps for each biopsy, the performance of the cribriform detection was assessed with receiver operating characteristic (ROC) and free-response receiver operating characteristic (FROC) analyses. To do so, cut-offs on the cribriform probability were varied to select the cribriform pixels. Thereafter, for each cut-off, neighboring cribriform pixels were taken together to form cribriform regions. The cribriform regions were analyzed in two ways: biopsy-wise and annotation-wise. The biopsy-wise analysis considered a biopsy positive for *reference* purposes if there was at least one annotation by the pathologists labelled as cribriform. Similarly, the *prediction* of a biopsy was considered positive if there were at least one predicted cribriform pixel in it. Complementary, the annotation-wise analysis considered an annotated (*reference*) cribriform region correctly detected if and only if at least one pixel of a *predicted* cribriform region overlapped with it. We performed both types of analyses while also studying the effect of only taking into account regions with a cumulative pixel area larger than 0.0150 mm^2 from both the predictions and the annotations. This size was chosen since the smallest cribriform region in the annotations was 0.0155 mm^2 .

Re-evaluation study

To increase our insight into wrong classifications of the network, the pathologists who made the initial annotations re-evaluated the false positive and false negative detected regions. While doing so, they were not informed of the classification outcome of the network nor of their own original annotation. From each false negative and false positive region a 512×512 patch was extracted surrounding the center of gravity of the region. Practically, this provided sufficient context for the pathologists to

Groups	1	2	3	4	5	6	7	8	Total
Number of biopsies	13	15	16	17	17	18	18	14	128
G3	124/13	121/14	106/14	124/16	78/16	143/18	132/15	148/14	976/120
G4 fused	24/7	9/5	22/8	20/4	26/9	27/8	48/12	21/5	197/58
G4 ill-defined	57/6	75/11	44/6	51/11	51/11	41/11	51/9	71/9	441/74
G4 complex fused	6/2	1/1	4/2	1/1	9/2	4/2	3/1	0/0	28/11
G4 glomeruloid	15/1	1/1	54/7	14/2	34/4	32/4	27/7	6/3	183/29
G4 cribriform	20/5	20/5	20/5	20/6	20/6	20/6	20/6	21/6	161/45

Table 2. Number of instances, i.e. regions/biopsies distributed over cross validation folds.

classify glands. For each such patch, the pathologists only re-evaluated the center. As with the original annotations, the same 7 labels could be assigned. Simultaneously, a confidence level had to be indicated on a scale from 0 (meaning undecided), to 4 (highly confident). Furthermore, if the pathologist was in doubt about the growth pattern, secondary labels could be registered. The outcomes were summarized in a confusion table.

Inter-observer study

The performance of our method in relation to the inter-observer variability of the gland pattern annotations was evaluated based on the data from the inter-observer study performed by Kweldam et al.⁵. This dataset contains 60 prostate histopathology images extracted after radical prostatectomies and was classified by 23 genitourinary pathologists. Kweldam et al.⁵ aimed to include 10 images classified as G3, 40 as G4 (10 per growth pattern) and 10 as G5. These were selected by two pathologists not involved in the subsequent assessment by the 23 raters. The selected prostate images were acquired with a NanoZoomer digital slide scanner (Hamamatsu Photonics, Hamamatsu City, Japan). To avoid ambiguity during the annotation, for each case a yellow line delineated the glands to be classified (Fig. 6).

We applied our neural network to this dataset and compared the cribriform detection with the assessments of the pathologists.

We trained 8 versions of our neural network with the dataset described previously in the section *Cribriform detection performance*. Following the distribution shown in table 2, each network was trained on 7 groups and one group was used to select 4 optimal neural network weights based on the validation metric V while applying different $\alpha \in [0.2, 0.3, 0.4, 1]$. We repeated this 4 times and iterating across the 8 groups to obtain in total 128 ($=4*4*8$) different neural networks. The ensemble of the 128 trained neural network was applied to each image of the inter-observer dataset.

To do so the images of this dataset were resampled to yield the same resolution as the training data: $0.92 \mu\text{m}/\text{pixel}$. The resulting images were fed in patches of 1024×1024 pixels into our networks (as above), after which only the predicted output within the contoured regions was retained. If at least one pixel in the output was predicted as cribriform with a probability superior to a particular cut-off (between 0 and 1), we considered that a cribriform growth pattern was detected. Cut-offs to be applied were chosen based on the FROC curve derived from the validation set used during the training.

Results

Cribriform detection performance

Fig. 2 shows the ROC curves representing the cribriform detection sensitivity as a function of false positive rate per *biopsy*. Complementary, it shows the FROC curves of the cribriform detection sensitivity per *annotation* as a function of the mean number of false positive detections in a non-cribriform biopsy.

In both figures, the dashed curves (and associated shaded areas) depict the mean performance (and corresponding standard deviation) concerning the 16 neural networks that were trained during each fold. Furthermore, solid curves represent the performances of the ensemble networks. The green curves collate results on all cribriform regions, whereas the blue curves consider only results of regions larger than 0.0150 mm^2 .

The area under the curve (AUC) of the ensemble network in the ROC curve was 0.80 with all regions and 0.82 for regions larger than 0.0150 mm^2 .

Several representative example images with predictions and annotations are presented in Fig. 3.

Re-evaluation study

In order to extract the false positive and negative regions of the ensemble network, we applied a cut-off to the cribriform prediction probability. We conveniently chose the cut-off to 0.5 (Fig. 2, right) in order to have a moderate amount of false positive regions to annotate, given the limited time the pathologists could allocate to this task. Applying the cut-off to the cribriform prediction probability yielded in total 632 false positive and 25 false negative cribriform region patches.

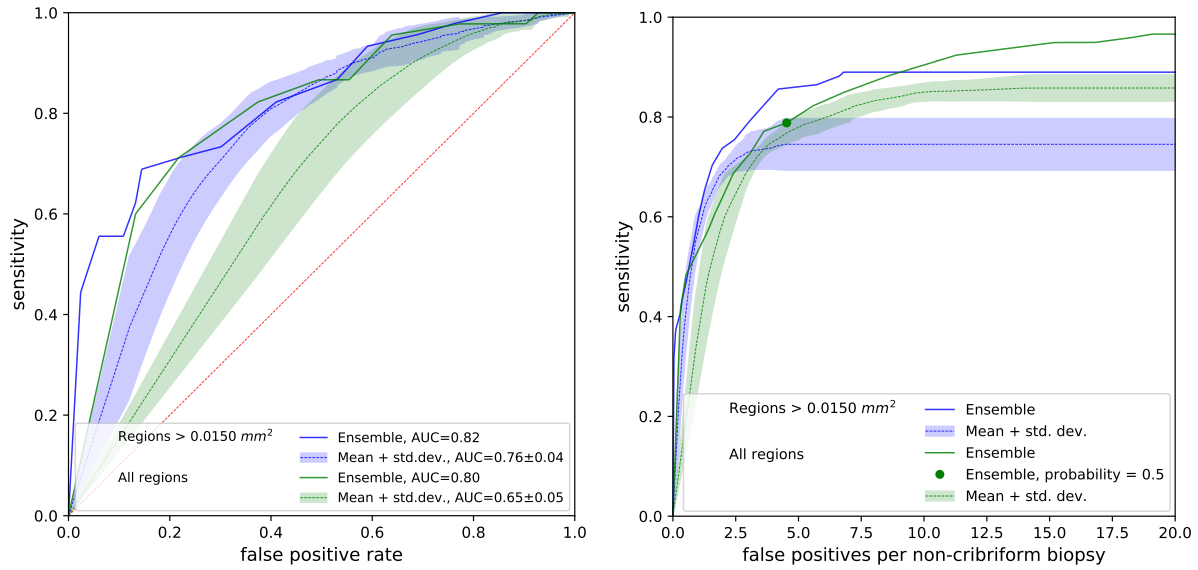


Figure 2. (left) Receiver operating characteristic (ROC) curves showing cribriform detection sensitivity per *biopsy* as a function of the false positive rate (i.e. 1-specificity). Dashed lines represent mean ROC curves from the 16 networks; the associated shaded areas represent the corresponding standard deviations. The solid lines derive from the ensemble networks. Green curves concern all cribriform regions, blue curves were based on regions larger than 0.0150 mm^2 . (right) Free-response receiver operating characteristic (FROC) curves of the cribriform detection sensitivity per *annotation* as a function of the average number of false positive predictions per non-cribriform biopsy. The green dot indicates, for the ensemble network with all regions, the cut-off probability of network output ($p = 0.5$) conveniently chosen for the re-evaluation experiment (see *Re-evaluation study* section).

During the re-evaluation, the pathologists gave ‘cribriform’ as the first label to $9\% (= 59/632)$ of the false positive patches. Furthermore, the pathologists indicated ‘cribriform’ as the first or second label (the ‘doubtful’ cases) to 20% of false positive patches.

At the same time, upon re-evaluation the pathologists did not indicate ‘cribriform’ as the first label in $44\% (= 11/25)$ of the false negative cases. Furthermore, the pathologists did not indicate ‘cribriform’ as the first nor as the second label in 16% of those cases.

For $71\% (= 468/657)$ of the wrongly classified patches (taking false positives and negatives together), the originally given label was identical to the first label during re-evaluation. Furthermore, in 48% of the false positive patches and 36% of the false negative patches, no second label was given.

The median confidence level was 4 (highly confident) for patches with same labels during the initial annotation and the first annotation of the re-evaluation. The median confidence level was 2 for patches labeled differently as such. Furthermore, confidence level 4 was given to 51% of the false positive patches and 28% of the false negative patches during re-evaluation.

An overview of the initial annotations and first label during re-evaluation of the false positives and false negatives is contained in the confusion matrix in Fig. 4. Additionally, the figure shows examples of the false positive and negative cases including details on the annotations by the pathologist.

Inter-observer study

Fig. 5 shows the FROC curve of the ensemble network generated based on the evaluation set of the training data by varying the probability threshold. In order to compare the performance of the ensemble network to the assessments by the 23 pathologist we applied three probability thresholds/cut-offs: (1) 0.0125 corresponding to the highest attained sensitivity on the evaluation set; (2) 0.1 at which level 95% sensitivity is reached; (3) 0.5 at which level 85% sensitivity is reached.

Top-right and bottom-right charts in Fig. 5 show the number of regions predicted as *cribriform* and *not cribriform* respectively by the neural network as a function of the percentage of pathologists annotating these images as cribriform.

Observe that there are 9, 3 and 0 regions labelled as cribriform by the network applying the thresholds at 0.0125, 0.1 and 0.5, respectively, which no pathologist annotated as cribriform. These could be considered as false positive cases. Furthermore, the 21, 27 and 30 regions with the same thresholds labelled as not-cribriform by the network nor labelled as cribriform by any pathologist could be considered true negatives. The bottom-right chart in Fig. 5 demonstrates that with the cut-off at 0.0125 *all*

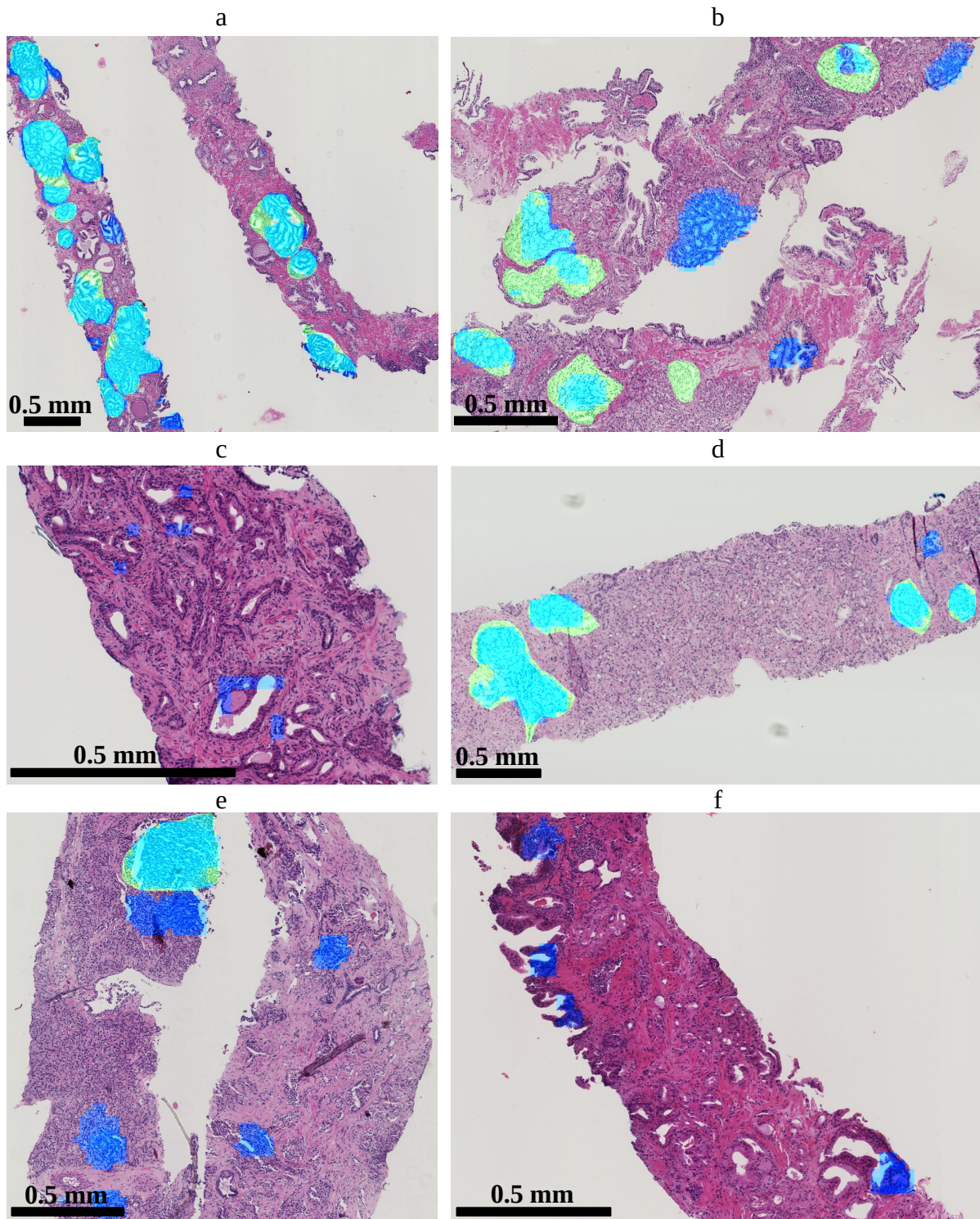


Figure 3. Biopsy slides with overlays showing predicted regions by the ensemble network as well as annotations (serving as reference). Light blue indicates true positive predictions; green are false negative regions; dark blue are false positive predictions. The scale of the images differs merely for illustration purposes.

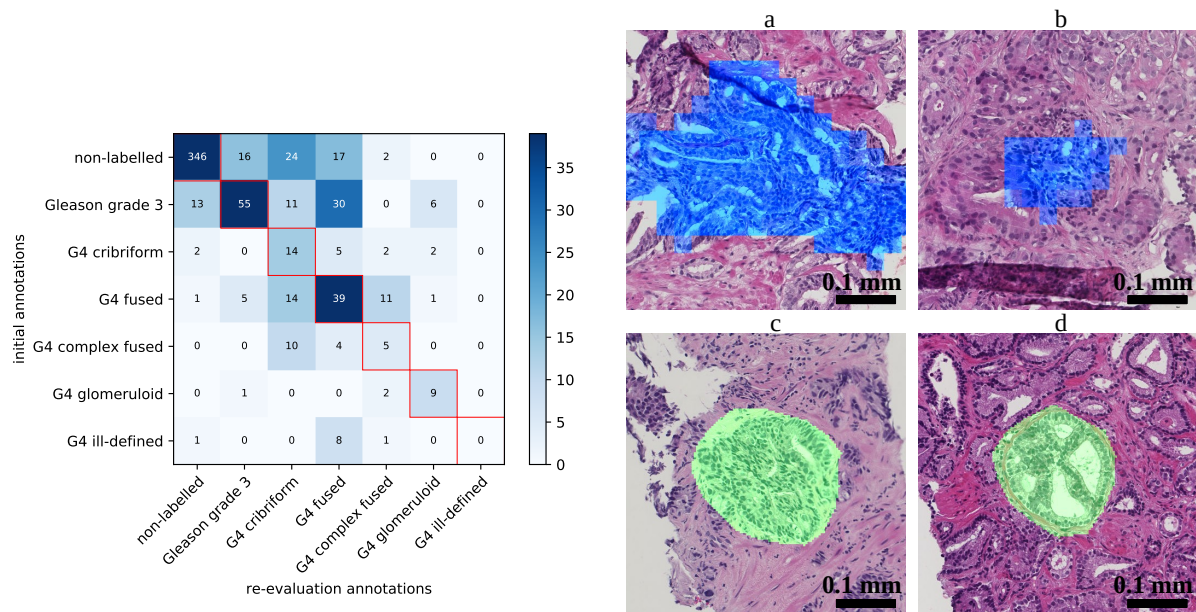


Figure 4. (left) Confusion matrix showing initial label versus first label during re-evaluation attributed by the pathologists to false positive and false negative patches.

(right) Example false positive and false negative cases re-evaluated by the pathologists. Blue indicates a false positive detection and green indicates a false negative annotation. (a) False positive patch initially annotated as ‘fused’ and given ‘cribriform’ as the first label during re-evaluation. (b) False positive patch initially annotated as ‘fused’ and given ‘complex fused’ as the first label and ‘cribriform’ as the second label during re-evaluation. (c) False negative patch initially annotated as ‘cribriform’ and ‘fused’ during re-evaluation. (d) False negative patch annotated as ‘cribriform’ both during initial annotation and re-evaluation. Observe that the automatic segmentations (top) are coarse because the output of the neural network is 32 times smaller than the input; annotations (bottom) were manually drawn on the originals and are therefore smoother.

the images annotated as cribriform by more than 30% ($\geq 7/23$) of the pathologists are predicted as cribriform by the neural network. Increasing the threshold to 0.1 and 0.5 leads to more regions not classified as cribriform and simultaneously less false positives. It may be noted that for 63% ($=19/30$) of the cribriform cases, less than 60% of the pathologists agreed regarding the labeling.

The average of Cohen’s kappa coefficient across all paired pathologist labelings is 0.62. The average of Cohen’s kappa coefficient between our method and each pathologist is 0.29, 0.36 and 0.39 at cut-offs of 0.0125, 0.1 and 0.5, respectively.

Fig. 6 shows example images for varying agreements between the pathologists on which the cribriform regions detected by the neural network are overlaid.

Discussion

We proposed a method to automatically detect and localize G4 cribriform growth patterns in prostate biopsy images based on convolutional neural networks. In order to improve the detection of cribriform growth patterns the network was trained to detect other growth patterns (complex fused, glomeruloid, ...) as well. Furthermore, to enhance the stability of the prediction, an ensemble of networks was trained after which the average prediction was used.

The ensemble network focusing on regions larger than 0.015 mm^2 reached an area under the curve of 0.82 regarding detection of biopsy images harboring a cribriform region. The FROC analysis showed that achieving a sensitivity of 0.9 for regions larger than 0.0150 mm^2 goes at the expense of on average 6.8 false positives per non-cribriform biopsy.

The training with the 16 different neural networks resulted in quite large standard deviations on the ROC and FROC curves. This could be an indication that the training data order influences the performance of the network. Our solution to cope with this was to apply the ensemble of neural networks. An alternative solution could be hard negative mining by prioritizing negative and difficult regions during the training. Yet another solution would be to acquire a larger training set, to take into account the heterogeneity of the data in a better way.

During the evaluation of the method, the variations among pathologists regarding cribriform growth pattern recognition was also studied. In particular, false positive and false negative patches from the ensemble classifier were re-evaluated by the same

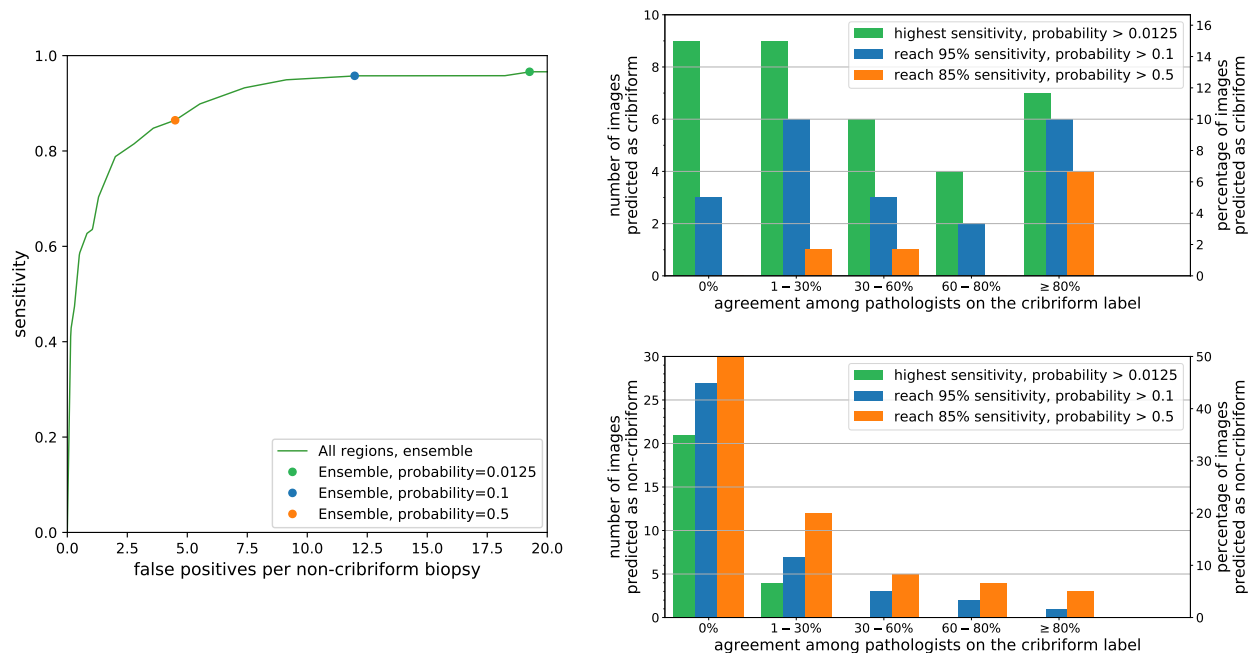


Figure 5. (left) Free-response receiver operating characteristic (FROC) curves of the cribriform detection sensitivity per *annotation* as function of the average number of false positive predictions per non-cribriform biopsy. This curve was resulted from the evaluation set using the ensemble of neural networks trained for the inter-observer study. The green dot corresponds with a probability cut-off at 0.0125, at which point the highest sensitivity is attained. The blue and orange dots correspond to probability cut-off at 0.1 and 0.5 yielding 95% and 85% sensitivity, respectively. (top-right) Numbers of images predicted as *cribriform* by the neural network as a function of the percentage of pathologists labeling these images as cribriform. (bottom-right) Numbers of images *not* predicted as cribriform by the neural network as a function of the percentage of pathologists labeling these images as cribriform.

pathologists.

The evaluation of the method with the original annotations showed that sensitive cribriform region detection can be done, but at the expense of a high number of false positives. However, the re-evaluation study demonstrated that up to 20% of the false positive detections could actually be cribriform regions. Concurrently, it showed that up to 44% of the false negatives might not be cribriform regions.

We also tested the ensemble network on a dataset annotated by 23 pathologists to put its performance into perspective regarding inter-observer variability. In 63% of the cases, less than 60% of the pathologists agreed regarding the cribriform labeling. Using a probability cut-off at 0.0125 (corresponding to the highest sensitivity in the training set) *all* images annotated as cribriform by at least 30% of the pathologists were also predicted as cribriform by the neural network. In other words, the network is rather conservative in classifying regions as cribriform even with a low percentage of agreement, which is opposed to detecting only regions for which there is large agreement. This is also reflected by the Cohen's kappa which showed higher agreement amongst pathologist than between our method and the pathologists. As such, with the cut-off at 0.0125, the network is more inclusive than the consensus of pathologists. This could be clinically relevant as preferably no potentially cribriform region should be missed by the automated detection algorithm at this stage.

There were typical false positive cribriform detections. First, as malignant glands are not properly attached to the surrounding stroma, tearing may happen during tissue processing. Figs 6.c and 6.d show resulting retraction and slit-like artifacts surrounded by cells with clear cytoplasm. The resulting background could be mistaken for cribriform lumina by the network. Second, in Figs 3.c and 3.f, some regions in non-labelled tissue have complex anastomosing glands, not meeting the criteria for cribriform growth. Finally, in the latter figure, the background seems confused by the network for cribriform lumina. Since these areas are but a small part of the total area of non-labelled tissue it could be that the network might not have seen sufficient examples of such patterns during the training.

The latter observation signifies the importance of diversity in the training data also for our application. Inclusion of healthy

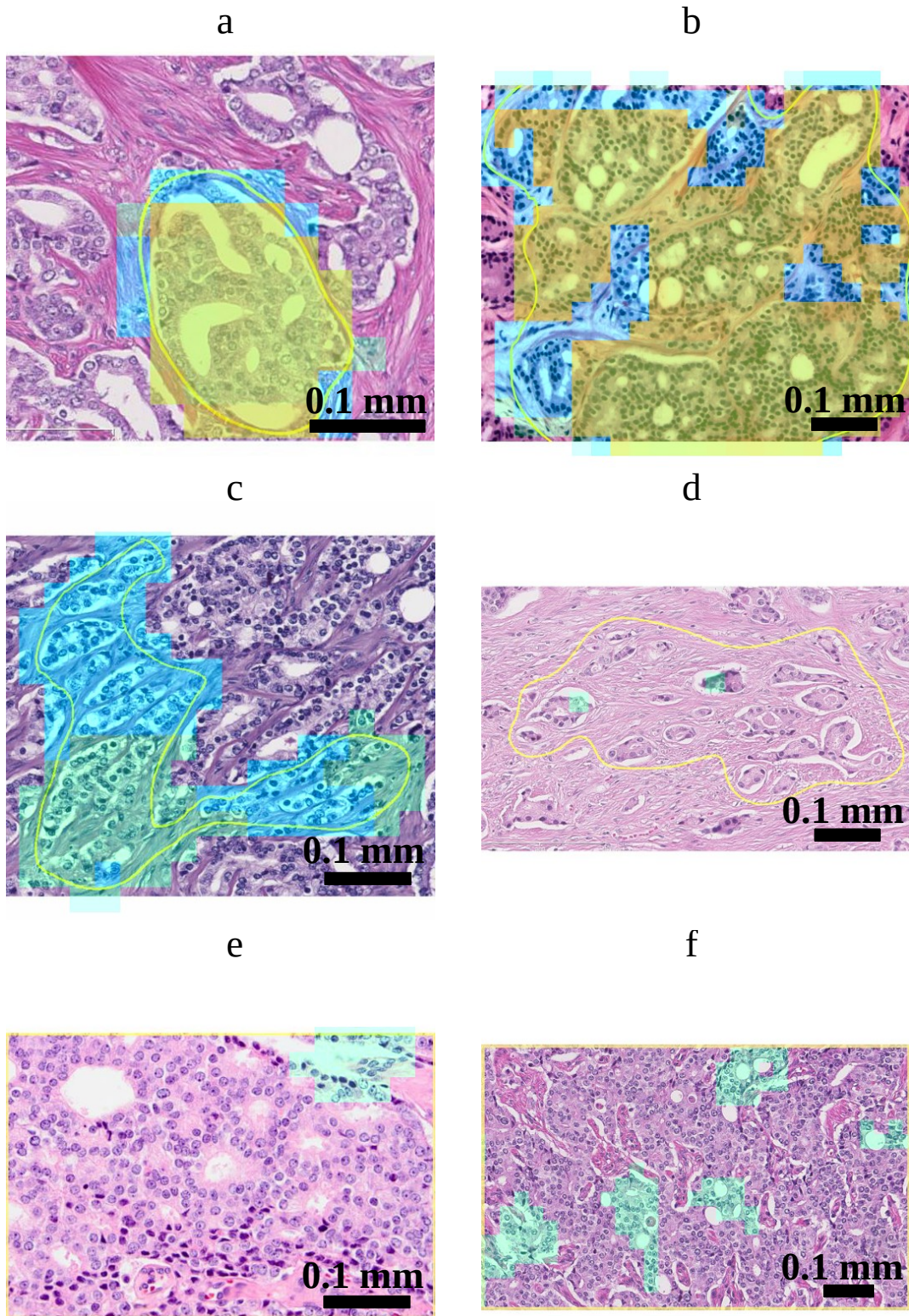


Figure 6. Cribriform growth pattern detection on images from the dataset of Kweldam et al.⁵. The yellow contours delineate the regions that were assessed by the pathologists. Green, blue and orange colors correspond to detection of cribriform regions at probability thresholds of 0.0125, 0.1 and 0.5 respectively. (a),(b) Images annotated as cribriform by 22 and 23 pathologists, respectively. (c),(d) Images annotated principally as ill-defined and as G3, respectively (no cribriform annotation). (e),(f) Images annotated as cribriform by 22 and 8 pathologists, respectively. Image (f) was annotated as fused by 13 pathologists. Note that the yellow contours for images (e) and (f) is at the image border.

tissue simultaneously with rare tissues such as G5, mucinous, and perineural structures are indispensable in the training set. For similar reasons, an important direction for future work could be to particularly focus on multi-center data. Also, annotations from multiple pathologists might help to build a more detailed probabilistic model and cover the variability from large consensus to large ambiguity. Previously, such approaches were proposed by Nir et al.¹⁰ for Gleason grading and by Kohl et al.²⁷ for segmentation of lung abnormalities.

A limitation of our study is that the pathologists were not aware that the cases presented in the re-evaluation study concerned erroneous classifications by the network. Since we did not include true positive and true negative cases nor indicated so to the pathologists, this might have biased their interpretation. As such, a further limitation is that a re-evaluation of positives cases is lacking. Furthermore, as it is stated in Kweldam et al.⁵, the dataset from the inter-observer study has been deliberately chosen to be difficult which may lead to more disagreement between pathologists than with biopsy analyses during daily clinical practice. The performance of the neural network is also impacted by this as such uncommon cases were not present in the training.

Our method could be used by pathologists as an automatic sanity check in order to quickly look at suspicious areas. For clinical decision making, a quantitative model could combine multiple image modalities such as prostate magnetic resonance imaging and biopsies with biomarkers including our cribriform detection.

Conclusion

We proposed a convolutional neural network to automatically detect and localize cribriform growth patterns in prostate biopsy images. The ensemble network reached an area under the curve of up to 0.82 for detection of biopsies harboring cribriform tissue. This result must be valued taking into account the large disagreement among pathologists. The network is showing rather conservative performance: cases were detected as cribriform even when just a limited number of pathologists labelled them as such. The method could be clinically useful by serving as a sanity check, to avoid missing cribriform patterns.

References

1. American Cancer Society. <https://www.cancer.org>.
2. Chen, N. & Zhou, Q. The evolving gleason grading system. *Chin. J. Cancer Res.* **28**, 58 (2016).
3. Epstein, J. I. *et al.* The 2014 international society of urological pathology (isup) consensus conference on gleason grading of prostatic carcinoma. *The Am. journal surgical pathology* **40**, 244–252 (2016).
4. Kweldam, C., van Leenders, G. & van der Kwast, T. Grading of prostate cancer: a work in progress. *Histopathology* **74**, 146–160 (2019).
5. Kweldam, C. F. *et al.* Gleason grade 4 prostate adenocarcinoma patterns: an interobserver agreement study among genitourinary pathologists. *Histopathology* **69**, 441–449 (2016).
6. Kweldam, C. F. *et al.* Cribriform growth is highly predictive for postoperative metastasis and disease-specific death in gleason score 7 prostate cancer. *Mod. pathology* **28**, 457 (2015).
7. Kweldam, C. F. *et al.* Disease-specific survival of patients with invasive cribriform and intraductal prostate cancer at diagnostic biopsy. *Mod. Pathol.* **29**, 630 (2016).
8. Hollemans, E. *et al.* Large cribriform growth pattern identifies isup grade 2 prostate cancer at high risk for recurrence and metastasis. *Mod. Pathol.* **32**, 139 (2019).
9. Gertych, A. *et al.* Machine learning approaches to analyze histological images of tissues from radical prostatectomies. *Comput. Med. Imaging Graph.* **46**, 197–208 (2015).
10. Nir, G. *et al.* Automatic grading of prostate cancer in digitized histopathology images: Learning from multiple experts. *Med. image analysis* **50**, 167–180 (2018).
11. Litjens, G. *et al.* A survey on deep learning in medical image analysis. *Med. image analysis* **42**, 60–88 (2017).
12. Arvaniti, E. *et al.* Automated gleason grading of prostate cancer tissue microarrays via deep learning. *Sci. reports* **8** (2018).
13. Ing, N. *et al.* Semantic segmentation for prostate cancer grading by convolutional neural networks. In *Medical Imaging 2018: Digital Pathology*, vol. 10581, 105811B (International Society for Optics and Photonics, 2018).
14. Nagpal, K. *et al.* Development and validation of a deep learning algorithm for improving gleason scoring of prostate cancer. *npj Digit. Medicine* **2**, 48 (2019).
15. Litjens, G. *et al.* Deep learning as a tool for increased accuracy and efficiency of histopathological diagnosis. *Sci. reports* **6**, 26286 (2016).

16. Campanella, G., Silva, V. W. K. & Fuchs, T. J. Terabyte-scale deep multiple instance learning for classification and localization in pathology. *arXiv preprint arXiv:1805.06983* (2018).
17. Lucas, M. *et al.* Deep learning for automatic gleason pattern classification for grade group determination of prostate biopsies. *Virchows Arch.* 1–7 (2019).
18. Li, J. *et al.* An attention-based multi-resolution model for prostate whole slide imageclassification and localization. *arXiv preprint arXiv:1905.13208* (2019).
19. Bulten, W. *et al.* Automated deep-learning system for gleason grading of prostate cancer using biopsies: a diagnostic study. *The Lancet Oncol.* (2020).
20. Gertych, A. *et al.* Convolutional neural networks can accurately distinguish four histologic growth patterns of lung adenocarcinoma in digital slides. *Sci. reports* **9**, 1483 (2019).
21. He, K., Zhang, X., Ren, S. & Sun, J. Deep residual learning for image recognition. In *Proceedings of the IEEE conference on computer vision and pattern recognition*, 770–778 (2016).
22. Springenberg, J., Dosovitskiy, A., Brox, T. & Riedmiller, M. Striving for simplicity: The all convolutional net. In *ICLR (workshop track)* (2015).
23. Hu, J., Shen, L. & Sun, G. Squeeze-and-excitation networks. In *Proceedings of the IEEE conference on computer vision and pattern recognition*, 7132–7141 (2018).
24. Glorot, X. & Bengio, Y. Understanding the difficulty of training deep feedforward neural networks. In *Proceedings of the thirteenth international conference on artificial intelligence and statistics*, 249–256 (2010).
25. Computation Pathology Group, Radboud University Medical Center. ASAP: Automated Slide Analysis Platform. <https://github.com/computationalpathologygroup/ASAP>.
26. Maier, B. F. binpacking python package. <https://github.com/benmaier/binpacking>.
27. Kohl, S. *et al.* A probabilistic u-net for segmentation of ambiguous images. In *Advances in Neural Information Processing Systems* **31**, 6965–6975 (2018).

Acknowledgements

This work was funded by the Netherlands Organization for Scientific Research (NWO), project TNW 15173. We thank NVIDIA Corporation for the donation of a Titan Xp via the GPU Grant Program. Muhammad Arif and Jifke Veenland of the Erasmus University Medical Center are acknowledged for fruitful discussions and advice.

Author contributions statement

P.A. designed and performed the algorithms and experiments, analyzed the results and wrote the manuscript. E.H. and G.J.L.H.L. performed the data collection, grading of the biopsy set and brought medical expertise. C.F.K. performed the data collection of the inter-observer set and brought medical expertise. S.S. and F.V. supervised the work and wrote the manuscript. All authors reviewed and revised the manuscript.

Additional information

Competing interests The authors declare no conflict of interest.